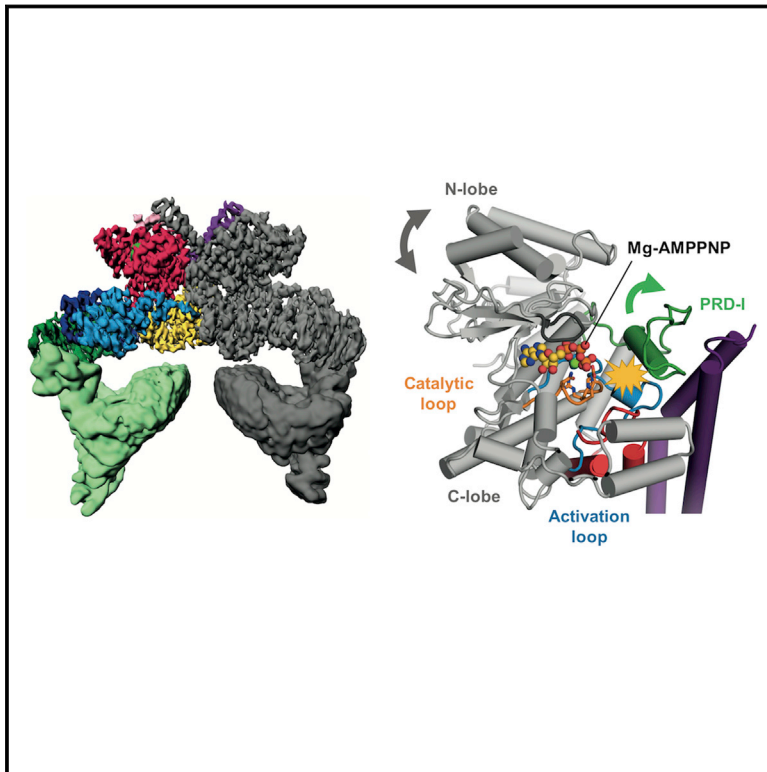


# Structure

## Cryo-EM Structure of Nucleotide-Bound Tel1<sup>ATM</sup> Unravels the Molecular Basis of Inhibition and Structural Rationale for Disease-Associated Mutations

### Graphical Abstract



### Authors

Luke A. Yates, Rhys M. Williams, Sarem Hailemariam, Rafael Ayala, Peter Burgers, Xiaodong Zhang

### Correspondence

xiaodong.zhang@imperial.ac.uk

### In Brief

Yates et al. describe the cryo-EM structure of Tel1 kinase in a nucleotide-bound state. The 3.7 Å structure provides a structural basis for its intrinsically low basal activity and a potential allosteric activation mechanism, and further provides insight into the occurrence of many disease-associated mutations of its human ortholog ATM.

### Highlights

- cryo-EM structure of Tel1 in complex with Mg<sup>2+</sup>-AMP-PNP at 3.7 Å resolution
- Key residues of the active site are in productive conformation for catalysis
- PIKK regulatory domain insert (PRD-I) restricts peptide substrate access
- Structural rationale for mutations found in ataxia-telangiectasia and cancer



# Cryo-EM Structure of Nucleotide-Bound Tel1<sup>ATM</sup> Unravels the Molecular Basis of Inhibition and Structural Rationale for Disease-Associated Mutations

Luke A. Yates,<sup>1,3</sup> Rhys M. Williams,<sup>1,3</sup> Sarem Hailemariam,<sup>2</sup> Rafael Ayala,<sup>1</sup> Peter Burgers,<sup>2</sup> and Xiaodong Zhang<sup>1,4,\*</sup>

<sup>1</sup>Section of Structural and Synthetic Biology, Faculty of Infectious Diseases, Imperial College London, London SW7 2AZ, UK

<sup>2</sup>Department of Biochemistry and Molecular Biophysics, Washington University School of Medicine, St Louis, MO 63110, USA

<sup>3</sup>These authors contributed equally

<sup>4</sup>Lead Contact

\*Correspondence: [xiaodong.zhang@imperial.ac.uk](mailto:xiaodong.zhang@imperial.ac.uk)

<https://doi.org/10.1016/j.str.2019.10.012>

## SUMMARY

Yeast Tel1 and its highly conserved human ortholog ataxia-telangiectasia mutated (ATM) are large protein kinases central to the maintenance of genome integrity. Mutations in ATM are found in ataxia-telangiectasia (A-T) patients and ATM is one of the most frequently mutated genes in many cancers. Using cryoelectron microscopy, we present the structure of Tel1 in a nucleotide-bound state. Our structure reveals molecular details of key residues surrounding the nucleotide binding site and provides a structural and molecular basis for its intrinsically low basal activity. We show that the catalytic residues are in a productive conformation for catalysis, but the phosphatidylinositol 3-kinase-related kinase (PIKK) regulatory domain insert restricts peptide substrate access and the N-lobe is in an open conformation, thus explaining the requirement for Tel1 activation. Structural comparisons with other PIKKs suggest a conserved and common allosteric activation mechanism. Our work also provides a structural rationale for many mutations found in A-T and cancer.

## INTRODUCTION

*Saccharomyces cerevisiae* Tel1 and its highly conserved human ortholog ataxia-telangiectasia mutated (ATM), are major kinases responsible for maintaining genome integrity. Tel1<sup>ATM</sup> is recruited to sites of DNA damage by the MRX/N complex, a key element in double-strand DNA (dsDNA) break repair comprising Mre11, Rad50, and Xrs2 (Nbs1 in human) (Falck et al., 2005). MRX/N is also the major activator of Tel1<sup>ATM</sup>, which subsequently phosphorylates hundreds of targets that contain an S/T-Q motif (Lee and Paull, 2004; Matsuoka et al., 2007; Lee and Paull, 2005; Lee et al., 2003; Uziel et al., 2003). Many of these targets, including CHK1/2, ATM, BRCA1, PALB2, p53, and H2AX, are tumor suppressors involved in cell-cycle control and dsDNA break repair through homologous recombination (Lavin and Kozlov, 2007; Matsuoka et al., 2007). The precise mechanism of Tel1<sup>ATM</sup> activation is not fully understood, but is sug-

gested to involve autophosphorylation (Kozlov et al., 2006), lysine acetylation (Sun et al., 2005), and dissociation of homodimers into monomers (Bakkenist and Kastan, 2003). Critically, mutations in ATM are found in ataxia-telangiectasia (A-T), a rare disease primarily associated with immunodeficiency and progressive neurological decline. A-T patients also have an increased susceptibility to malignancy due to genomic instability, and ATM is one of the most frequently mutated genes in many cancers (Choi et al., 2016).

Tel1<sup>ATM</sup> belongs to a family of phosphatidylinositol 3-kinase (PI3K)-like kinases that also includes ATR (ATM-Rad3-related, and its yeast ortholog Mec1), DNA-PKc, mammalian target of rapamycin (mTOR), TRRAP/Tra1, and SMG1 (Baretic and Williams, 2014). All PI3K kinases contain a canonical two-lobed kinase domain, with the smaller N-lobe containing the highly conserved glycine-rich loop (Gly-rich loop), while the larger C-lobe possesses the catalytic and activation loops (Walker et al., 1999). A number of additional conserved and functional elements within the kinase domain have been identified in phosphatidylinositol 3-kinase-related kinases (PIKKs) including the LST8-binding element (LBE) (Yang et al., 2013) and the PIKK regulatory domain (PRD) (Mordes et al., 2008). Flanking the kinase domain are the N-terminal HEAT repeats, followed by a FAT (FRAP [FKBP12-rapamycin-associated protein], ATM, TRRAP [transformation/transcription domain-associated protein]) domain and a ~35-residue FATC domain at the C terminus (Imseng et al., 2018). Due to their large sizes, structural and mechanistic studies on these kinases have been challenging. A number of high-resolution structures (<4.0 Å, where many side chains can be resolved) are available, mostly of those involving mTOR, including its complexes with a number of activator proteins (Yang et al., 2017). The 4.3-Å crystal structure of DNA-PKcs revealed the architecture of this large PIKK (Sibanda et al., 2017), whereas the 3.9-Å cryoelectron microscopy (cryo-EM) structure of Mec1-Ddc2 provided a structural basis for how ATR<sup>Mec1</sup> might be kept in an inhibited state (Wang et al., 2017). The cryo-EM structures of Tel1 (Xin et al., 2019) and human ATM (Baretic et al., 2017) in the absence of nucleotides have shed some light into kinase function, but do not provide a complete understanding of the role of the regulatory elements in maintaining an auto-inhibited state.

Here we present the cryo-EM structure of *Saccharomyces cerevisiae* Tel1 in complex with an ATP analog, AMP-PNP, with sufficient resolution (3.7–3.9 Å) to resolve the bound nucleotide and allow most of the side chains in the conserved



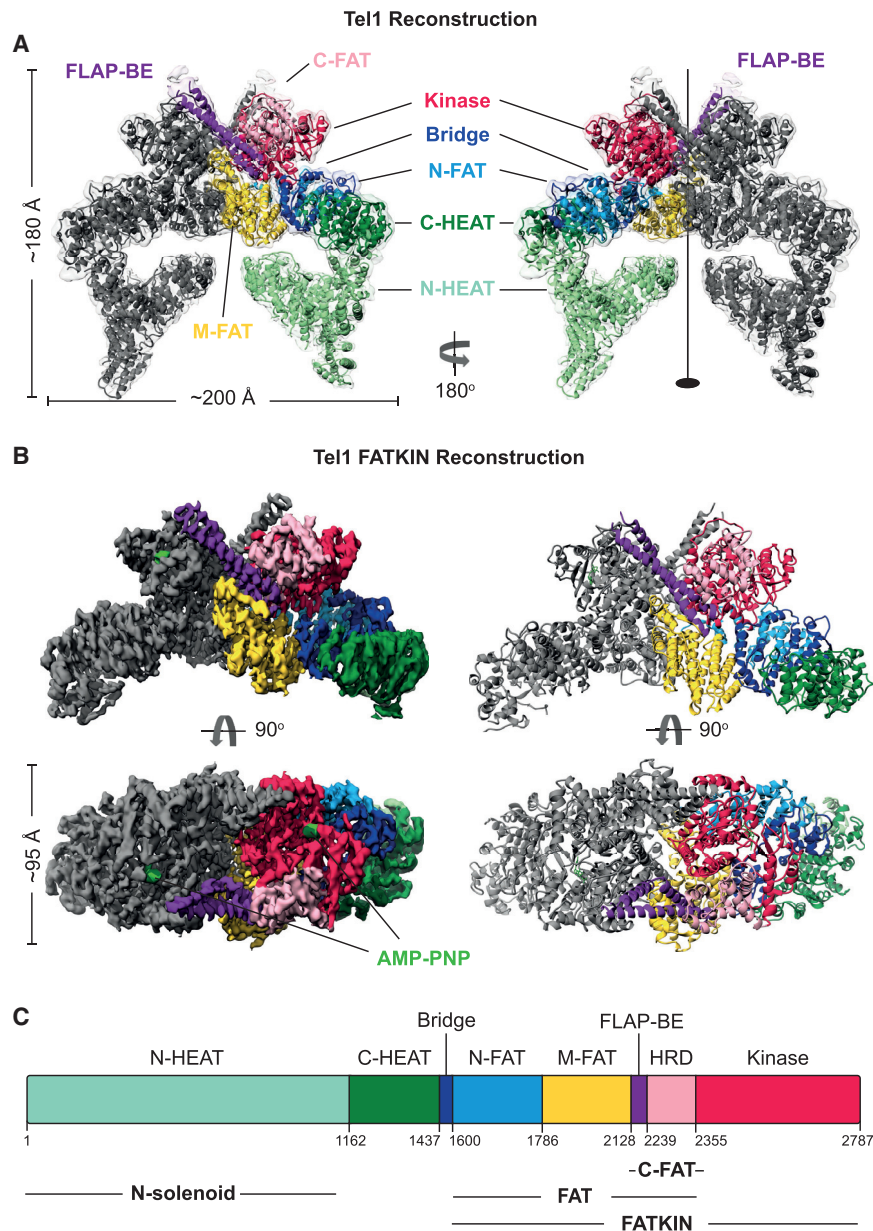


**Figure 1. Structure of Tel1 Dimer**

(A) Overall structure of the nucleotide-bound (AMP-PNP) Tel1 dimer structure determined by cryo-EM to 3.9 Å resolution by Gold Standard Fourier shell correlation (GS-FSC). Regions of the structure are colored according to domains; kinase, red; C-FAT, pink; FLAP-BE, purple; N-FAT, blue; bridge, dark blue; C-HEAT, green; N-HEAT, light green. Approximate dimensions of the protein are also given.

(B) Reconstruction of the FAT-KIN region determined to 3.7 Å resolution by GS-FSC, colored as in (A).

(C) Domain arrangement of Tel1. See also [Figures S1](#) and [S2](#).

synergistically by both dsDNA and MRX ([Hailemariam et al., 2019](#)). The overall Tel1 dimer structure was refined to a global resolution of 3.9 Å ([Figures S1](#) and [S2](#) and [Table 1](#)). Using localized masking around density regions corresponding to the FAT-KIN domains as well as regions of HEAT repeats and/or signal subtractions to isolate the FAT-KIN domains improved the quality of the map to 3.7 Å for these regions, which correspond to two-thirds of the whole protein ([Figure S3](#)). In key functional regions around the kinase domain and the dimer interface, the local resolution estimates are better than 3.5 Å; and densities for bulky side chains are clearly visible ([Figure S2](#)). Consequently, we could build side chains into the majority of the FAT, kinase, and FATC domains (residues 1,527–2,787) and place confident sequence assignment between residues 968 and 1,526. The N-terminal HEAT repeats are flexible, as was also shown in ATM structures, and left as  $C\alpha$  trace only due to the lack of clear side-chain density. Our structure is in excellent agreement with that of an ATM closed

dimer, which was limited to  $C\alpha$ - $C\beta$  atoms ([Baretić et al., 2017](#)). Interestingly, we did not observe an open dimer conformation or monomers in our analysis ([Figure S2](#)), although N-HEAT domains are mobile ([Figure S1](#)).

FAT-kinase-FATC (FAT-KIN) to be resolved ([Figures 1](#), [S1](#), and [S2](#) and [Table 1](#)). Significantly, a conserved insertion in the PRD-I obscures peptide substrate access to the active site. This explains the low intrinsic activity of Tel1 and its requirement for activation by the binding of MRX and DNA. Due to the high degree of structural conservation between ATM and the Tel1 FAT-KIN regions, where a large number of pathogenic mutations are located, our structure also provides a structural basis for many disease mutations found in ATM.

## RESULTS AND DISCUSSION

### Structure of the Tel1 Dimer

Tel1 was expressed and purified as reported previously ([Sawicka et al., 2016](#)), and its kinase activity shown to be stimulated

Different subdomain terminologies have been used to describe PIKKs, including ATM. For simplicity, we use rigid bodies to define subdomains within the HEAT repeats and the FAT domain, which was originally assigned by multiple sequence alignments ([Bosotti et al., 2000](#)). Specifically, by comparing the structure of Tel1 and those of ATM and mTOR, the N-terminal HEAT repeats can be separated into two rigid bodies, which we term N-HEAT (residues 1–1,162) and C-HEAT (residues 1,163–1,437) ([Figure 1](#)). There is a connecting region, denoted a bridge domain (residues 1,438–1,600) before the FAT domain, which we have extended and also divided into several rigid bodies: N-FAT (N-terminal FAT,

**Table 1. Data Collection and Refinement Statistics**

Data Acquisition			
Dataset no.	Dataset 1	Dataset 2	Dataset 3
Sample	Tel1-AMP-PNP		
Microscope	Titan KRIOS (eBIC, Oxfordshire, UK)		
Voltage (kV)	300	300	300
No. of micrographs	4,508	2,445	5,656
Nominal magnification	75,000 (129,032)	75,000 (129,032)	75,000 (129,032)
Detector	Falcon III (linear mode)	Falcon III (linear mode)	Falcon III (linear mode)
Pixel size (Å/pix)	1.085	1.085	1.085
Dose rate (e <sup>-</sup> /Å <sup>2</sup> /s)	105	120	102
Frames (e <sup>-</sup> /Å <sup>2</sup> /frame)	23 (3.8)	34 (2.6)	34 (2.6)
Total dose (e <sup>-</sup> /Å <sup>2</sup> )	88.8	88.4	88.9
Integration time (s)	0.59	0.87	0.87
Defocus range	-1.1 to -3.2	-1.1 to -3.2	-1.2 to -3.2
Image Processing			
Reconstruction	Tel1 dimer (EMD-10120)	FAT-KIN (EMD-10120)	
Software	RELION-3.0		
Particles	167,596		
Box size (pixels)	380 × 380 × 380		
Symmetry	C2		
Map resolution (Å)	3.9		
Map resolution range (Å)	3.6–5.6		
Map sharpening B factor (Å <sup>2</sup> )	-75		
	-165		
Coordinate Refinement			
Software	PHENIX		
Algorithm	REAL SPACE REFINEMENT		
Resolution (Å)	4.0		
FSC <sub>model vs. map</sub> = 0.5 (Å)	4.1		
Correlation coefficient	0.84		
	0.81		
Model			
PDB	6S8F		
No. of residues			
Protein	5,158 (2,579 per monomer)		
Ligand (AMP-PNP)	2 (1 per monomer)		
B factors overall	243.7 (82.2 for FAT-KIN)		
Protein	243.7 (82.2 for FAT-KIN)		
AMP-PNP	223.3 (79.0 for FAT-KIN)		
Root-mean-square deviation			

Bond length (Å)	0.006
Bond angle (°)	0.99
Validation	
MolProbity score	1.86
MolProbity clash score	5.87
Rotamer outliers (%)	0.8
C <sub>β</sub> deviations (%)	0
Ramachandran plot (%)	
Favored	90.4
Allowed	9.5
Outliers	0.1

1,600–1,786), M-FAT (Middle-FAT, 1,787–2,128) and C-FAT (C-terminal FAT, 2,129–2,355) (Figures 1 and S3). The C-FAT consists of the FLAP-BE (as defined in Baretic et al., 2017) and HRD domain (Figure 1).

The Tel1 dimer interface is extensive and can be divided into three layers (Figure 2A); the top layer consists of PRD-I and LBE of one protomer interacting with a long helical antenna specific to Tel1<sup>ATM</sup> called FLAP-BE, of the adjacent protomer (FLAP-BE', where ' denotes elements from the adjacent protomer) (Figure 2); the middle layer mainly consists of FATC of one protomer and the adjacent M-FAT' (immediately preceding FLAP-BE) of the other protomer, while the bottom layer consists of M-FAT-M-FAT' interactions (Figure 2A). The buried surface area at the dimer interface is extensive, with over 3,000 Å<sup>2</sup> per protomer. The bottom layer of the dimer interface is exclusively hydrophobic in nature, with a vast array of large bulky hydrophobic residues (Phe and Leu) forming a well-buried core around the 2-fold symmetry axis (Figure 2B). The middle layer employs a mixture of polar and hydrophobic residues (Figure 2C), whereas the upper layer, which has the smallest interface surface area and is the least well resolved, interacts via charge complementarity (Figure 2D). The hydrophobic nature of the bottom layer enables some conformational flexibility at the bottom layer of the dimer interface, whereas the top layer, which is polar in nature, can be broken or rearranged. Indeed, a relative rotation of the FAT-KIN regions in the ATM dimer has been observed in the open dimer conformation (Baretic et al., 2017).

### Tel1 Nucleotide-Bound Kinase Domain Is in a Catalytically Productive Conformation

Similar to the other PIKKs such as mTOR, ATM, DNA-PKc, and Mec1, the kinase domain is surrounded by the FAT domains that form a C-shaped cradle surrounding the kinase domain (Figure 3A). It is worth noting that N-FAT contacts the kinase C-lobe, whereas C-FAT contacts the N-lobe (Figures 1A and 3A). M-FAT sits away from the kinase domain and instead contacts C-HEAT and is in close proximity with N-HEAT and could therefore transmit conformational changes from the HEAT region to the kinase domain (Figures 1A and 3A).

The structure of nucleotide-bound Tel1 shows the catalytic residues of the C-lobe in a catalytically productive conformation, with clear density for AMP-PNP (Figures 3B and 3C). The catalytic loop, containing the highly conserved <sup>2612</sup>DRH<sup>2614</sup> motif, adopts a similar conformation to that observed in mTOR

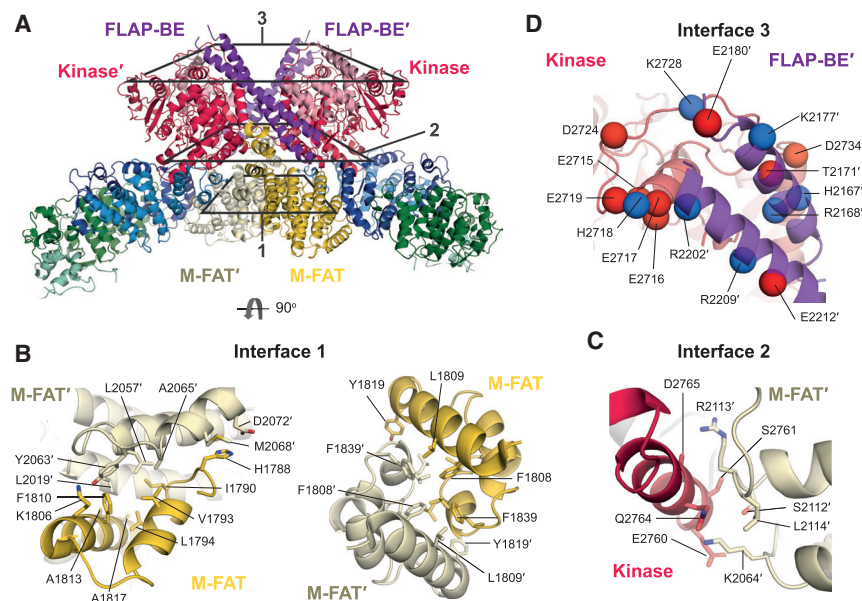


**Figure 2. Tel1 Dimer Interface**

(A) FAT-KIN dimer structure colored by domain as in Figure 1, and for clarity M-FAT' is colored in pale yellow to distinguish it clearly. Different layers of the dimer interface are boxed and detailed views of the nature of the interface are shown in (B)–(D). See also Figure S3.

Tel1 active site with nucleotide-bound mTOR in non-activated and RHEB-activated states (Yang et al., 2017) shows that the N-lobe and the Gly-rich loop of Tel1 most closely resemble that of non-activated mTOR (Figure S5). Further closure of the mTOR N-lobe and Gly-rich loop occur upon activation. Therefore, it is likely that the N-lobe and Gly-rich loop of Tel1 will also undergo further closure as part of the catalytic cycle. In addition to the Gly-rich loop, the active site is further surrounded by LBE, PRD, and

FLAP-BE' (Figure 3), highlighting the importance of these elements in regulating active site access.

### Tel1<sup>ATM</sup> PRD-I and FATC Regulate Substrate Binding

In addition to the open N-lobe, our structure shows that the active site cleft of the Tel1 kinase domain is restricted by the PRD, which we have denoted as the PRD-I (see below, Figure 3B). The PRD is a PIKK-specific feature that was originally identified in ATR as an element between the kinase domain and the FATC that is essential for the binding of the activator TopBP1 (Mordes et al., 2008). Subsequent PIKK structures have revealed that the regions proposed to be involved in TopBP1 binding are in the highly conserved K $\alpha$ 10 helix, whereas the regions between K $\alpha$ 9 and K $\alpha$ 10 are variable in length and composition between different PIKKs (Figure 3E). Therefore, we denote this variable region as the PRD-I, which is equivalent to K $\alpha$ 9b, K $\alpha$ 9c, and K $\alpha$ 9d identified in mTOR and ATM structures (Baretić et al., 2017; Yang et al., 2013, 2017).

In the nucleotide-free Tel1 and ATM symmetric dimer structures, the PRD-I, although only partly resolved, is predicted to occupy the position of a peptide substrate (Baretić et al., 2017; Xin et al., 2019). In the nucleotide-bound Tel1 structure, the complete PRD-I could be resolved. It structurally connects K $\alpha$ 9-K $\alpha$ 10 at the back of the kinase domain to the LBE and FATC at the front of the kinase domain (Figure 3B). Starting from K $\alpha$ 9, the PRD-I displays an extended loop followed by a single  $\alpha$  helix, situated directly above the activation loop, reaching toward LBE and FLAP-BE' before returning to K $\alpha$ 10 via a loop (Figure 3B). Importantly, PRD-I interacts with many of the key functional and structural elements, including the activation loop, the FATC, the LBE, and the FLAP-BE' (Figures 3B and 3D). At its N terminus, an invariant W2702 of PRD-I inserts into the hydrophobic pocket between K $\alpha$ 9 and K $\alpha$ 10 (Figure 3B). Toward the C-terminal end, acidic residues in PRD-I (<sup>2715</sup>EEEHE<sup>2719</sup>) are in close proximity to a positively charged patch in FLAP-BE' (<sup>2197</sup>KRHYHR<sup>2202</sup>) (Figure 2D). Together these elements occlude the access to the active site of Tel1.

structures (Figures S2 and S4) (Yang et al., 2013, 2017), where D2612 is well-positioned to act as the catalytic base for deprotonation of the hydroxyl group from a bound peptide substrate. The side chains of H2614 and N2616, important for stabilizing transition state during phosphoryl transfer, co-ordinate the  $\gamma$ -phosphate of AMP-PNP (Figures 3B, 3C, S2G, and S2H) (Bao et al., 2011; Madhusudan et al., 2002; Yang et al., 2013). The Mg<sup>2+</sup>-binding N2617 of the catalytic loop, the <sup>2631</sup>DLG<sup>2633</sup> motif, and the adjacent activation loop are well-ordered, allowing us to model in one Mg<sup>2+</sup> ion coordinating the  $\beta$ -/ $\gamma$ - (Mg1) of AMP-PNP into the density, using nucleotide-bound structures of protein kinase A (PKA), CDK2, and mTORC1 as a guide (Figures 3B, S2G, and S2H) (Das et al., 2015; Yang et al., 2013). There is also weak density at the correct position for a second Mg<sup>2+</sup>, although studies on CDK2 suggest binding of the second “activating” Mg<sup>2+</sup> is concomitant with substrate peptide binding (Bao et al., 2011). Whether this is the case also for Tel1 is unclear and we have therefore omitted the second Mg<sup>2+</sup> in our structural model. The activation loop, which is ordered in this kinase, wraps around the catalytic loop and supports kinase activity via several interactions. Most notably, residues E2646 and I2634 of the activation loop sandwich the catalytic loop, and there is an apparent interaction between R2613 of the catalytic loop (<sup>2612</sup>DRH<sup>2614</sup> motif) and the main chain of the activation loop, close to the <sup>2631</sup>DLG<sup>2633</sup> motif. The catalytic loop is further constrained by two aromatic residues (W2783 and Y2787) from the C terminus of FATC (Figure 3C). These structural constraints explain the highly conserved nature of FATC and why mutations in this region abolish Tel1<sup>ATM</sup> activity (Jiang et al., 2006).

The binding pocket for the adenosine ring of AMP-PNP is formed by a number of hydrophobic residues from both N- and C-lobes of the Tel1 kinase domain, with the Gly-rich loop from the N-lobe forming a partial lid over the bound nucleotide (Figures 3B and 3C). The conserved K2465 from the N-lobe contributes to  $\alpha$ -/ $\beta$ -phosphate coordination of the bound AMP-PNP and is equivalent to K72 of PKA, which is essential for catalysis (Iyer et al., 2005) (Figure 3B). Interestingly, comparison of the

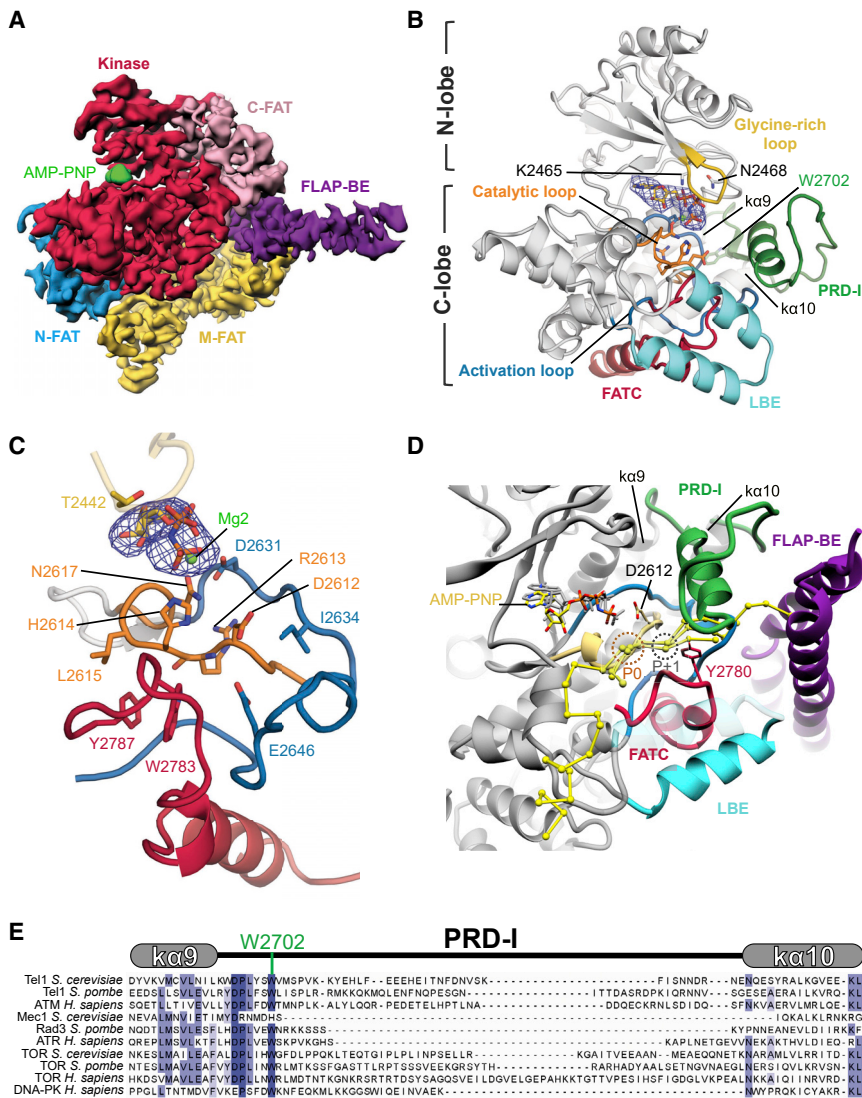


### Figure 3. Details of the Tel1 Kinase Domain and the PRD-I

(A) Cryo-EM density of Tel1 FAT-KIN shows the FAT domains cradle the kinase domain. Domains are colored as in Figure 1.

(B) Structural details of the AMP-PNP bound (with cryo-EM density shown as blue mesh) to the kinase domain (gray) with key structural features highlighted and labeled.

(C) Molecular details of interacting residues with AMP-PNP, the activation loop (blue) and FATC (red) which support the catalytic loop (yellow).

(D) Predicted peptide binding using superimposition of kinase-substrate peptide complex crystal structures of PKA, Pak-4, and Cdk2. The target serine/threonine is shown and labeled (P0) and the predicted location of the P+1 residue is highlighted and is close to Y2780 of the FATC.

(E) Sequence alignment of the structurally conserved  $\text{ka}9$  and  $\text{ka}10$  and the intervening PRD of several PIKKs. An invariable tryptophan (W2702) that anchors the PRD is highlighted.

See also Figures S4 and S5.

catalytic loop conformation as well as substrate peptide recognition.

### Proposed Activation Mechanism of Tel1<sup>ATM</sup>

Among the PIKK enzymes, only mTOR has a set of high-resolution structures of both non-active and activated states. Comparisons of mTORC1 and the activator-bound mTORC1-RHEB complex reveal that RHEB binding induces allosteric conformational changes to C-FAT that, via a clockwise rotation around the kinase C-lobe, results in the closure of the N-lobe and glycine-rich loop, thus realigning the active site (Yang et al., 2017).

To estimate the path of a bound Tel1 peptide substrate, we aligned the Tel1 kinase domain with the catalytic and activation loops of substrate-bound structures of PKA (PDB: 3x2u; Das et al., 2015), Cdk2 (PDB: 3qhw; Bao et al., 2011), and Pak-4 (PDB: 4jdh; Chen et al., 2014) (Figure 3D). It is clear that PRD-I in Tel1 overlaps with the peptide substrate binding site, whereas the  $\gamma$ -phosphate of AMP-PNP and the catalytic aspartate (D2612) are suitably close to the predicted location of the target Ser/Thr (P0) for phosphoryl transfer to occur (Das et al., 2015) (Figure 3D). The PRD-I, together with the LBE and FLAP-BE', thus occludes the active site and occupies the substrate binding site. Therefore, it is a major determinant for inhibition and the requirement of Tel1 activation by MRX-dsDNA. Furthermore, Y2780 within the FATC sits close to the predicted P+1 peptide substrate position, suggesting a potential role in determining substrate specificity. This is consistent with a Y2780A mutant Tel1 demonstrating significantly defective levels of Rad53 phosphorylation, supporting the idea that this part of FATC may be involved in target recognition (Ogi et al., 2015). Thus, we suggest a dual role for FATC, being important for constraining the

RHEB binds at a significant distance away from the kinase domain, close to N-FAT (Yang et al., 2017). Upon binding of RHEB, through HEAT domain relocation, significant conformational changes occur in M-FAT and are subsequently transmitted to C-FAT (Yang et al., 2017). DNA-PKcs also bind to its activator, Ku70-Ku80-DNA, through its HEAT repeats. Structural comparisons between mTOR and DNA-PKcs alone and in complex with their activators reveal a common mode of allosteric activation involving domain movement of M-FAT and C-FAT (Sharif et al., 2017; Sibanda et al., 2017; Yin et al., 2017). Despite the structural and sequence divergence of the N-HEAT region, the FAT-KIN domains of PIKKs are highly conserved in their structures (Figure S5). Furthermore, the conserved conformational changes in mTOR and DNA-PKc, irrespective of their distinct activator binding sites, suggest similar conformational changes might occur in Tel1 as a means for activation.

Tel1<sup>ATM</sup> interacts with MRX/N via direct associations with the complex (Lee and Paull, 2004), and recent studies suggest that each of the three MRX subunits binds Tel1, suggesting an extensive MRX-Tel1 interaction interface (Hailemariam et al., 2019).

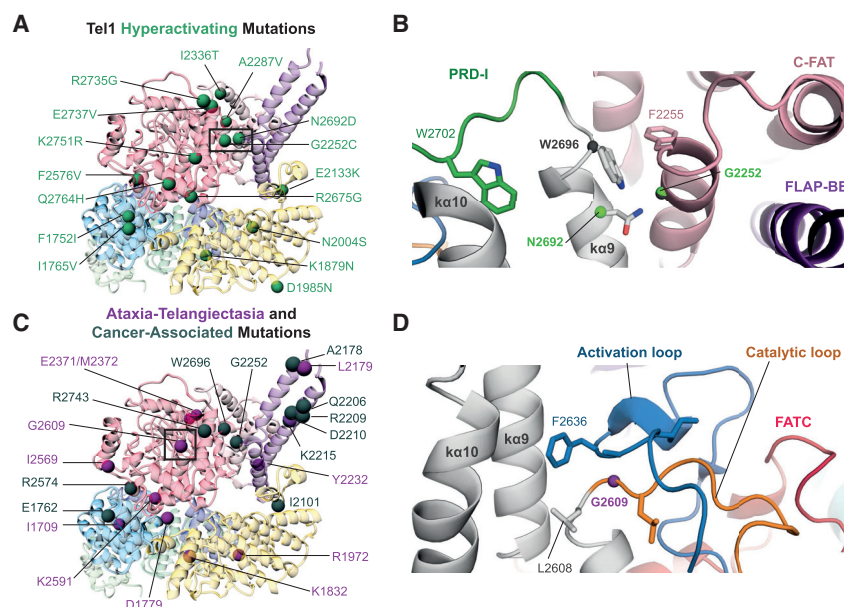


**Figure 4. Mapping of Tel1 Hyperactivating and ATM Disease-Associated Mutations**

(A) Tel1 FAT-KIN protomer is shown colored as in Figure 1 with hyperactivating mutations found in Baldo et al. (2008) mapped and shown as green spheres.

(B) Molecular details of a cluster of mutations in  $K\alpha 9$  found in cancer and described in hyperactivating Tel1 phenotypes.

(C) Cancer-associated (dark gray spheres) and ataxia-telangiectasia-associated (A-T, purple spheres) mutations at structurally equivalent locations (see Table S1 for details).

(D) Molecular details of G2609 (G2867 in ATM), which is mutated to arginine in A-T. See also Table S1.

The interaction between Tel1 and the C terminus of Xrs2/Nbs1 has been mapped to regions in the N-HEAT and C-HEAT domains in Tel1<sup>ATM</sup> (You et al., 2005) in a similar location to DNA-PK and mTORC1 activator binding sites (Figure S5). When we align the Tel1 and the inactive mTORC1 structures on their kinase C-lobes, N-FAT, and C-FAT align reasonably well, with the largest differences in M-FAT (Figure S5). Therefore, it is plausible that binding of MRN/X would result in a concerted motion of HEAT and M-FAT, which is propagated to C-FAT, resulting in the N-lobe and glycine-rich loop closure analogous to RHEB-activated mTORC1 (Yang et al., 2017). Distinct from mTOR, these movements would involve FLAP-BE within the C-FAT, which subsequently could affect PRD-I conformation and the dimer interface, presumably releasing inhibition for substrate binding and active site access.

In the apo-ATM and apo-Tel1 structures, both symmetric and asymmetric dimers were observed, with the ATM study suggesting that asymmetry is coupled with an increased basal activity *in vitro*. A recent study on apo-ATM also presents the existence of ATM monomers in their samples, which are also more active, although it is unclear if these monomers resulted directly from activation (Xiao et al., 2019). Indeed, given the characteristics of the Tel1 dimer interface observed in this study, it seems that a dimer-to-monomer transition would be energetically unfavorable with a free energy of dissociation ( $\Delta G^{\text{Diss}}$ ) of  $\sim 37$  kcal/mol calculated in PISA (Krissinel and Henrick, 2007). Asymmetric dimers for ATM and Tel1 have been associated with disordered PRD-I (Xin et al., 2019) and are proposed to be the active form or en-route to becoming active. If so, the activators' roles would be either to stabilize the asymmetric dimers or to induce the asymmetric dimers. This is not inconsistent with the proposed allosteric activation mechanism upon activator binding, which could induce or stabilize the asymmetric arrangement. However, our studies do not provide evidence for the existence of a substantially asymmetric arrangement within the FAT-KIN domains when Tel1 is bound to Mg-AMP-PNP. Furthermore, we did not observe similar

PRD-I disorder when Tel1 is nucleotide bound, and this is consistent with the low-level *in vitro* kinase activity of Tel1 in the absence of activators ( $\sim 0.065$  phosphates transferred per minute per protomer) (Hailemariam et al., 2019). Activator-bound structures are required in order to understand how these kinases are activated.

#### Structural Basis for Hyperactive Mutations of Tel1 and Disease-Associated Mutants in ATM

The role of PRD-I in inhibiting the activity of Tel1 and a proposed allosteric activation mechanism are supported by Tel1 hyperactive mutations identified in a genetic screen to rescue Mec1-deficient cells (Baldo et al., 2008). Many mutations are in similar positions to cancer-associated mTOR hyperactivating mutations known to increase sensitivity to allosteric activation (Yang et al., 2017). Several mutations map onto  $K\alpha 9$  and  $K\alpha 10$  and surrounding regions (Figure 4A). Among the mutant strains, three possess only single-amino acid substitutions (N2692D, F2576V, and Q2764H), that hyperactivate Tel1 activity. In one such mutant, N2692 of  $K\alpha 9$  is next to G2252 of C-FAT, which is also mutated in one of the strains, and therefore N2692D or G2252C could affect  $K\alpha 9$  conformation and consequently affect the PRD-I position (Figure 4B). Q2764 is within the FATC and also located at the dimer interface with M-FAT', specifically in a region just before the FLAP-BE'. A Q2672H substitution could affect FLAP-BE' to aid the relocation of PRD-I. There are also a number of mutations at the interface between N-FAT and C-lobe, close to the LBE and activation loop. These mutations could also affect substrate access (Figure 4A). Several mutations, e.g., I2336T and A2287V, are found within the C-FAT, close to the N-lobe and are similar to known mTOR hyperactivating mutations (Yang et al., 2017). Presumably these mutations could allow the N-lobe to move closer to the active site in the absence of activator proteins.

The high structural homology between Tel1 and ATM FAT-KIN regions allows us to map pathogenic A-T missense and cancer-associated mutations onto the structure (Figure 4C). A-T is caused by biallelic mutation of the ATM gene and a significant proportion of ATMs result in abolished ATM expression, via truncation, incorrect splicing, or incorrect frame-shifts (McKusick, 2007; Sandoval et al., 1999; Stankovic et al., 1998), suggesting

that the molecular basis of A-T is loss of ATM protein. The majority of A-T missense mutations are found within the FAT-KIN domains (Choi et al., 2016) and ATM is often mutated in multiple cancers, with the FAT-KIN regions exhibiting some of the highest mutational frequency (Forbes et al., 2015; McKusick, 2007). Consistent with loss of activity in A-T and possibly in some cancers, some of the cancer-associated mutations are present in the highly conserved Gly-rich loop, the catalytic loop, as well as the activation loop, thus affecting catalytic activity directly. A good example is the ATM G2867R (G2609 in Tel1), which sits within the catalytic loop at a sharp turn just below the activation loop (Figure 4D). The introduction of a large charged side chain would certainly alter the structure of these elements critical for catalysis.

A large number of disease-associated substitutions are found outside the kinase active site and are distributed within the FAT domain and kinase-FAT interface. Strikingly, there is a large cluster of mutations within the FLAP-BE and others around PRD-I, especially in K $\alpha$ 9 and K $\alpha$ 10 and regions surrounding them (Figure 4; Table S1). Presumably these mutations affect PRD-I, and thus substrate phosphorylation. The ATM, V2424G (L2179 in Tel1), sits close to the cancer-associated mutations E2423, R2443Q, E2444K, and D2448 $\Phi$  (A2178, Q2206, R2209, and D2210 in Tel1, respectively) (Figure 4C; Table S1) and are likely to disrupt the FLAP-BE structure as they hold the two helices together through salt bridges or hydrophobic interactions. Disrupting the FLAP-BE would likely alter the PRD-I within the context of a dimer and would therefore alter peptide substrate access. Another cluster of mutations exists around LBE and FATC. Mutations in these regions would also affect substrate access by affecting PRD-I. Interestingly, similar to hyperactive mutations, several pathogenic mutations are concentrated around the interfaces between the C-lobe and N-FAT; again these mutations could affect key elements including LBE and the activation loop or prevent allosteric activation.

The nucleotide-bound structure presented here reveals that Tel1 exists as an auto-inhibited dimer that is likely activated via an allosteric mechanism found in other PIKKs. With the exception of the N-lobe, the nucleotide coordinating residues and the catalytic site in the C-lobe are positioned or only require subtle rearrangement to allow catalysis. However, the PRD-I competes with peptide-substrates and occludes the access to the active site, and is likely the major determinant of the low basal activity of Tel1. The PRD-I is held in place by a number of PIKK-specific features, with mutations in these regions leading to altered activity and disease phenotypes. The movement of the PRD-I is clearly necessary for full kinase activity and based on other related PIKKs may occur through an allosteric mechanism that is common to this family of kinases. Hyperactivating mutations and disease-associated mutations of Tel1 and ATM clearly suggest the FAT domain is involved in regulating the activity of this kinase. Further structural work on an activator-bound Tel1<sup>ATM</sup> is required to resolve how the PRD-I is evicted from the active site to allow peptide substrate binding.

## STAR★METHODS

Detailed methods are provided in the online version of this paper and include the following:

- **KEY RESOURCES TABLE**
- **LEAD CONTACT AND MATERIALS AVAILABILITY**
- **METHOD DETAILS**
  - Electron Microscopy Grid Preparation
  - CryoEM Data Acquisition
  - CryoEM Image Processing
  - Model Building and Refinement
  - Model Interpretation and Analysis
- **QUANTIFICATION AND STATISTICAL ANALYSIS**
- **DATA AND CODE AVAILABILITY**

## SUPPLEMENTAL INFORMATION

Supplemental Information can be found online at <https://doi.org/10.1016/j.str.2019.10.012>.

## ACKNOWLEDGMENTS

Initial screening of samples was carried out at Imperial College London Center for Structural Biology EM facility. High-resolution data were collected at the eBIC (proposal EM19865), Diamond Light Source, and we thank Drs C. Alistair Seibert and Yuriy Chaban for their support in collecting the data. eBIC is funded by the Wellcome Trust, MRC, and BBSRC. This work is funded by the Wellcome Trust Investigator Award to X.Z. (210658/Z/18/Z), the NIH (GM118129 to P.B.) and an NSF Graduate Research Fellowship (2014157291 to S.H.).

## AUTHOR CONTRIBUTIONS

X.Z. and L.A.Y. designed the studies. S.H. and L.A.Y. prepared the samples. L.A.Y. with R.A. carried out initial cryo-EM studies. L.A.Y. and R.M.W. performed the cryo-EM analysis, and built and refined the structural models. X.Z. and P.B. supervised the studies. X.Z., L.A.Y., and R.M.W. wrote the manuscript with input from all the authors.

## DECLARATION OF INTERESTS

The authors declare no competing interests.

Received: June 28, 2019

Revised: September 5, 2019

Accepted: October 18, 2019

Published: November 15, 2019

## REFERENCES

- Adams, P.D., Afonine, P.V., Bunkóczi, G., Chen, V.B., Davis, I.W., Echols, N., Headd, J.J., Hung, L.W., Kapral, G.J., Grosse-Kunstleve, R.W., et al. (2010). PHENIX: a comprehensive Python-based system for macromolecular structure solution. *Acta Crystallogr. D Biol. Crystallogr.* **66**, 213–221.
- Afonine, P.V., Klaholz, B.P., Moriarty, N.W., Poon, B.K., Sobolev, O.V., Terwilliger, T.C., Adams, P.D., and Urzhumtsev, A. (2018). New tools for the analysis and validation of cryo-EM maps and atomic models. *Acta Crystallogr. D Struct. Biol.* **74**, 814–840.
- Bakkenist, C.J., and Kastan, M.B. (2003). DNA damage activates ATM through intermolecular autophosphorylation and dimer dissociation. *Nature* **421**, 499–506.
- Baldo, V., Testoni, V., Lucchini, G., and Longhese, M.P. (2008). Dominant TEL1-hy mutations compensate for Mec1 lack of functions in the DNA damage response. *Mol. Cell. Biol.* **28**, 358–375.
- Bao, Z.Q., Jacobsen, D.M., and Young, M.A. (2011). Briefly bound to activate: transient binding of a second catalytic magnesium activates the structure and dynamics of CDK2 kinase for catalysis. *Structure* **19**, 675–690.
- Baretić, D., and Williams, R.L. (2014). PIKKs—the solenoid nest where partners and kinases meet. *Curr. Opin. Struct. Biol.* **29**, 134–142.

- Baretic, D., Pollard, H.K., Fisher, D.I., Johnson, C.M., Santhanam, B., Truman, C.M., Kouba, T., Fersht, A.R., Phillips, C., and Williams, R.L. (2017). Structures of closed and open conformations of dimeric human ATM. *Sci. Adv.* **3**, e1700933.
- Bosotti, R., Isacchi, A., and Sonnhammer, E.L. (2000). FAT: a novel domain in PIK-related kinases. *Trends Biochem. Sci.* **25**, 225–227.
- Chen, C., Ha, B.H., Thévenin, A.F., Lou, H.J., Zhang, R., Yip, K.Y., Peterson, J.R., Gerstein, M., Kim, P.M., Filippakopoulos, P., et al. (2014). Identification of a major determinant for serine-threonine kinase phosphoacceptor specificity. *Mol. Cell* **53**, 140–147.
- Chen, V.B., Wedell, J.R., Wenger, R.K., Ulrich, E.L., and Markley, J.L. (2015). MolProbity for the masses-of data. *J. Biomol. NMR* **63**, 77–83.
- Choi, M., Kippis, T., and Kurzrock, R. (2016). ATM mutations in cancer: therapeutic implications. *Mol. Cancer Ther.* **15**, 1781–1791.
- Das, A., Gerlits, O., Parks, J.M., Langan, P., Kovalevsky, A., and Heller, W.T. (2015). Protein kinase a catalytic subunit primed for action: time-lapse crystallography of Michaelis complex formation. *Structure* **23**, 2331–2340.
- Emsley, P., and Cowtan, K. (2004). Coot: model-building tools for molecular graphics. *Acta Crystallogr. D Biol. Crystallogr.* **60**, 2126–2132.
- Falck, J., Coates, J., and Jackson, S.P. (2005). Conserved modes of recruitment of ATM, ATR and DNA-PKcs to sites of DNA damage. *Nature* **434**, 605–611.
- Forbes, S.A., Beare, D., Gunasekaran, P., Leung, K., Bindal, N., Boutselakis, H., Ding, M., Bamford, S., Cole, C., Ward, S., et al. (2015). COSMIC: exploring the world's knowledge of somatic mutations in human cancer. *Nucleic Acids Res.* **43**, D805–D811.
- Hailemariam, S., Kumar, S., and Burgers, P.M. (2019). Activation of Tel1<sup>ATM</sup> kinase requires Rad50 ATPase and long nucleosome-free DNA, but no DNA ends. *J. Biol. Chem.* **294**, 10120–10130.
- Imseng, S., Aylett, C.H., and Maier, T. (2018). Architecture and activation of phosphatidylinositol 3-kinase related kinases. *Curr. Opin. Struct. Biol.* **49**, 177–189.
- Iyer, G.H., Garrod, S., Woods, V.L., and Taylor, S.S. (2005). Catalytic independent functions of a protein kinase as revealed by a kinase-dead mutant: study of the Lys72His mutant of cAMP-dependent kinase. *J. Mol. Biol.* **351**, 1110–1122.
- Jiang, X., Sun, Y., Chen, S., Roy, K., and Price, B.D. (2006). The FATC domains of PIKK proteins are functionally equivalent and participate in the Tip60-dependent activation of DNA-PKcs and ATM. *J. Biol. Chem.* **281**, 15741–15746.
- Kozlov, S.V., Graham, M.E., Peng, C., Chen, P., Robinson, P.J., and Lavin, M.F. (2006). Involvement of novel autophosphorylation sites in ATM activation. *EMBO J.* **25**, 3504–3514.
- Krissinel, E., and Henrick, K. (2007). Inference of macromolecular assemblies from crystalline state. *J. Mol. Biol.* **372**, 774–797.
- Lavin, M.F., and Kozlov, S. (2007). ATM activation and DNA damage response. *Cell Cycle* **6**, 931–942.
- Lee, J.H., and Paull, T.T. (2004). Direct activation of the ATM protein kinase by the Mre11/Rad50/Nbs1 complex. *Science* **304**, 93–96.
- Lee, J.H., and Paull, T.T. (2005). ATM activation by DNA double-strand breaks through the Mre11-Rad50-Nbs1 complex. *Science* **308**, 551–554.
- Lee, J.H., Xu, B., Lee, C.H., Ahn, J.Y., Song, M.S., Lee, H., Canman, C.E., Lee, J.S., Kastan, M.B., and Lim, D.S. (2003). Distinct functions of Nijmegen breakage syndrome in ataxia telangiectasia mutated-dependent responses to DNA damage. *Mol. Cancer Res.* **1**, 674–681.
- Madhusudan, Akamine, P., Xuong, N.H., and Taylor, S.S. (2002). Crystal structure of a transition state mimic of the catalytic subunit of cAMP-dependent protein kinase. *Nat. Struct. Biol.* **9**, 273–277.
- Matsuoka, S., Ballif, B.A., Smogorzewska, A., McDonald, E.R., Hurov, K.E., Luo, J., Bakalarski, C.E., Zhao, Z., Solimini, N., Lerenthal, Y., et al. (2007). ATM and ATR substrate analysis reveals extensive protein networks responsive to DNA damage. *Science* **316**, 1160–1166.
- McKusick, V.A. (2007). Mendelian inheritance in man and its online version, OMIM. *Am. J. Hum. Genet.* **80**, 588–604.
- Mordes, D.A., Glick, G.G., Zhao, R., and Cortez, D. (2008). TopBP1 activates ATR through ATRIP and a PIKK regulatory domain. *Genes Dev.* **22**, 1478–1489.
- Ogi, H., Goto, G.H., Ghosh, A., Zencir, S., Henry, E., and Sugimoto, K. (2015). Requirement of the FATC domain of protein kinase Tel1 for localization to DNA ends and target protein recognition. *Mol. Biol. Cell* **26**, 3480–3488.
- Pei, J., and Grishin, N.V. (2007). PROMALS: towards accurate multiple sequence alignments of distantly related proteins. *Bioinformatics* **23**, 802–808.
- Pettersen, E.F., Goddard, T.D., Huang, C.C., Couch, G.S., Greenblatt, D.M., Meng, E.C., and Ferrin, T.E. (2004). UCSF Chimera—a visualization system for exploratory research and analysis. *J. Comput. Chem.* **25**, 1605–1612.
- Ramlaul, K., Palmer, C.M., and Aylett, C.H.S. (2019). A local agreement filtering algorithm for transmission EM reconstructions. *J. Struct. Biol.* **205**, 30–40.
- Sandoval, N., Platzer, M., Rosenthal, A., Dörk, T., Bendix, R., Skawran, B., Stuhmann, M., Wegner, R.D., Sperling, K., Banin, S., et al. (1999). Characterization of ATM gene mutations in 66 ataxia telangiectasia families. *Hum. Mol. Genet.* **8**, 69–79.
- Sawicka, M., Wanrooij, P.H., Darbari, V.C., Tannous, E., Hailemariam, S., Bose, D., Makarova, A.V., Burgers, P.M., and Zhang, X. (2016). The dimeric architecture of checkpoint kinases mec1atr and tel1atm reveal a common structural organization. *J. Biol. Chem.* **291**, 13436–13447.
- Sharif, H., Li, Y., Dong, Y., Dong, L., Wang, W.L., Mao, Y., and Wu, H. (2017). Cryo-EM structure of the DNA-PK holoenzyme. *Proc. Natl. Acad. Sci. U S A* **114**, 7367–7372.
- Sibanda, B.L., Chirgadze, D.Y., Ascher, D.B., and Blundell, T.L. (2017). DNA-PKcs structure suggests an allosteric mechanism modulating DNA double-strand break repair. *Science* **355**, 520–524.
- Sievers, F., Wilm, A., Dineen, D., Gibson, T.J., Karplus, K., Li, W., Lopez, R., McWilliam, H., Remmert, M., Söding, J., et al. (2011). Fast, scalable generation of high-quality protein multiple sequence alignments using Clustal Omega. *Mol. Syst. Biol.* **7**, 539.
- Stankovic, T., Kidd, A.M., Sutcliffe, A., McGuire, G.M., Robinson, P., Weber, P., Bedenham, T., Bradwell, A.R., Easton, D.F., Lennox, G.G., et al. (1998). ATM mutations and phenotypes in ataxia-telangiectasia families in the British Isles: expression of mutant ATM and the risk of leukemia, lymphoma, and breast cancer. *Am. J. Hum. Genet.* **62**, 334–345.
- Sun, Y., Jiang, X., Chen, S., Fernandes, N., and Price, B.D. (2005). A role for the Tip60 histone acetyltransferase in the acetylation and activation of ATM. *Proc. Natl. Acad. Sci. U S A* **102**, 13182–13187.
- Tan, Y.Z., Baldwin, P.R., Davis, J.H., Williamson, J.R., Potter, C.S., Carragher, B., and Lyumkis, D. (2017). Addressing preferred specimen orientation in single-particle cryo-EM through tilting. *Nat. Methods* **14**, 793–796.
- Uziel, T., Lerenthal, Y., Moyal, L., Andegeko, Y., Mittelman, L., and Shiloh, Y. (2003). Requirement of the MRN complex for ATM activation by DNA damage. *EMBO J.* **22**, 5612–5621.
- Walker, E.H., Perisic, O., Ried, C., Stephens, L., and Williams, R.L. (1999). Structural insights into phosphoinositide 3-kinase catalysis and signalling. *Nature* **402**, 313–320.
- Wang, X., Ran, T., Zhang, X., Xin, J., Zhang, Z., Wu, T., Wang, W., and Cai, G. (2017). 3.9 Å structure of the yeast Mec1-Dcc2 complex, a homolog of human ATR-ATRIP. *Science* **358**, 1206–1209.
- Xiao, J., Liu, M., Qi, Y., Chaban, Y., Gao, C., Pan, B., Tian, Y., Yu, Z., Li, J., Zhang, P., et al. (2019). Structural insights into the activation of ATM kinase. *Cell Res.* **29**, 683–685.
- Xin, J., Xu, Z., Wang, X., Tian, Y., Zhang, Z., and Cai, G. (2019). Structural basis of allosteric regulation of Tel1/ATM kinase. *Cell Res.* **29**, 655–665.
- Yang, H., Rudge, D.G., Koos, J.D., Vaidialingam, B., Yang, H.J., and Pavletich, N.P. (2013). mTOR kinase structure, mechanism and regulation. *Nature* **497**, 217–223.

- Yang, H., Jiang, X., Li, B., Yang, H.J., Miller, M., Yang, A., Dhar, A., and Pavletich, N.P. (2017). Mechanisms of mTORC1 activation by RHEB and inhibition by PRAS40. *Nature* 552, 368–373.
- Yin, X., Liu, M., Tian, Y., Wang, J., and Xu, Y. (2017). Cryo-EM structure of human DNA-PK holoenzyme. *Cell Res.* 27, 1341–1350.
- You, Z., Chahwan, C., Bailis, J., Hunter, T., and Russell, P. (2005). ATM activation and its recruitment to damaged DNA require binding to the C terminus of Nbs1. *Mol. Cell. Biol.* 25, 5363–5379.
- Zhang, K. (2016). Gctf: real-time CTF determination and correction. *J. Struct. Biol.* 193, 1–12.
- Zheng, S.Q., Palovcak, E., Armache, J.P., Verba, K.A., Cheng, Y., and Agard, D.A. (2017). MotionCor2: anisotropic correction of beam-induced motion for improved cryo-electron microscopy. *Nat. Methods* 14, 331–332.
- Zivanov, J., Nakane, T., Forsberg, B.O., Kimanius, D., Hagen, W.J., Lindahl, E., and Scheres, S.H. (2018). New tools for automated high-resolution cryo-EM structure determination in RELION-3. *Elife* 7, <https://doi.org/10.7554/eLife.42166>.
- Zivanov, J., Nakane, T., and Scheres, S.H.W. (2019). A Bayesian approach to beam-induced motion correction in cryo-EM single-particle analysis. *IUCrJ* 6, 5–17.

## STAR★METHODS

## KEY RESOURCES TABLE

REAGENT or RESOURCE	SOURCE	IDENTIFIER
Chemicals, Peptides, and Recombinant Proteins		
Tel1 (expressed in <i>Saccharomyces cerevisiae</i> )	(Hailemariam et al., 2019)	N/A
Adenylyl-imidodiphosphate (AMP-PNP Lithium salt)	Merck	Cat #10102547001
Deposited Data		
Tel1-AMPPNP complex coordinates	This work	PDB:6S8F
Tel1-AMPPNP complex reconstruction	This work	EMD-10120
Tel1 reconstruction (initial model)	(Sawicka et al., 2016)	EMD-4097
ATM	(Baretić et al., 2017)	PDB:5NP0
mTORC1-RHEB complex	(Yang et al., 2017)	PDB:6BCU
mTOR Kinase	(Yang et al., 2013)	PDB:4JSV
Protein Kinase A (PKA)	(Das et al., 2015)	PDB:3X2U
Cdk2	(Bao et al., 2011)	PDB:3QHW
Mec1-Ddc2	(Wang et al., 2017)	PDB:5X6O
DNA-PKcs	(Sibanda et al., 2017)	PDB:5LUQ
Experimental Models: Organisms/Strains		
<i>Saccharomyces cerevisiae</i> : strain background: PY265	(Hailemariam et al., 2019)	N/A
Recombinant DNA		
pBL602 (GST-Tel1 under Gal promoter)	(Sawicka et al., 2016)	N/A
Software and Algorithms		
RELION-3.0	(Zivanov et al., 2018)	N/A
Chimera	(Pettersen et al., 2004)	N/A
MotionCor2	(Zheng et al., 2017)	N/A
Coot	(Emsley and Cowtan, 2004)	N/A
Phenix real space refine	(Afonine et al., 2018)	N/A
Gctf	(Zhang, 2016)	N/A
Gautomatch	<a href="https://www.mrc-lmb.cam.ac.uk/kzhang/">https://www.mrc-lmb.cam.ac.uk/kzhang/</a>	N/A
LAFTER	(Ramlaul et al., 2019)	N/A
Graphpad Prism 8	N/A	N/A
PROMALS3D	(Pei and Grishin, 2007)	N/A
PISA	(Krissinel and Henrick, 2007)	N/A
PyMOL	Schrodinger, LLC, NY, USA	N/A
Clustal Omega	(Sievers et al., 2011)	N/A
MOLPROBITY	(Chen et al., 2015)	N/A
Other		
EM Grids (Lacey Formvar/Carbon, 300 mesh, Au)	Ted Pella	Cat #0182G

## LEAD CONTACT AND MATERIALS AVAILABILITY

Further information and requests for resources and reagents should be directed to and fulfilled by the Lead Contact, Xiaodong Zhang ([xiaodong.zhang@imperial.ac.uk](mailto:xiaodong.zhang@imperial.ac.uk)).

## METHOD DETAILS

## Electron Microscopy Grid Preparation

A frozen aliquot of *Saccharomyces cerevisiae* Tel1 (800nM, stored in 40mM HEPES 7.8, 10% Glycerol, 200mM NaCl, 2mM DTT, 0.1% Tween-20, 0.01% NP40, 1mM EDTA, 0.5mM EGTA) was diluted 8-fold using sequential addition of 10  $\mu$ l volumes of buffer (50mM

Tris-HCl, 50mM NaCl, pH 7.4 supplemented with AMP-PNP and Magnesium Acetate), and was incubated for 30 minutes on ice. The final concentration of Tel1 was 100nM; 1mM AMP-PNP; 4mM Mg(OAc)<sub>2</sub>. Samples (4  $\mu$ l) were deposited onto Lacey Carbon 300 mesh gold grids that also have an additional ultrathin carbon support layer (Ted Pella Inc. USA), which were plasma-cleaned, for 30 seconds in air, prior to sample application. Samples were vitrified in liquid ethane at liquid nitrogen temperature using a Vitrobot Mk IV (FEI) set with a blotting force of -6, a waiting time of 60 s and a blotting time of 2 seconds. Plunge freezing was performed at 4°C and 100% humidity.

### CryoEM Data Acquisition

High-resolution data were collected for Tel1 over three sessions at eBIC (Oxfordshire, UK) on an FEI Titan KRIOS (Thermo Fisher) and are summarised in [Table 1](#). For all three datasets, the microscopes were operated at 300kV with the specimen at cryogenic temperatures (approximately -180°C) with images recorded at 1-3  $\mu$ m underfocus on a Falcon III direct electron detector in linear mode at a nominal magnification of 75,000 X, corresponding to a calibrated pixel size of 1.09 Å, and a cumulative total electron dose of  $\sim 90 e^-/\text{Å}^2$ . We collected a total of 12,609 micrographs, which were fractionated into frames (dataset 1, 4508, 23 frames; dataset 2; 2445, 34 frames; dataset 3; 5656, 34 frames). A representative micrograph is shown in [Figure S1A](#).

### CryoEM Image Processing

Movie frames were aligned, corrected for drift, beam induced motion and dose-weighted using MotionCor2 ([Zheng et al., 2017](#)) using a 5 x 5 patch implemented in RELION-3.0 ([Zivanov et al., 2018](#)). Contrast transfer function (CTF) fitting was performed using Gctf ([Zhang, 2016](#)). Particles were picked with Gautomatch using re-projections of a low resolution Tel1 EM structure ([Sawicka et al., 2016](#)) for selection. Particles were extracted in RELION-3.0 using a box size of 400 x 400 pixels and binned four times for initial processing. The number of particles picked per dataset are summarised in [Table 1](#). Reference-free 2D classification of particles from a single dataset was performed in RELION-3.0 and revealed two major views ([Figure S1A](#)) and subsequent 3D volumes after refinement showed preferential orientation issues. Therefore, 2D classification was omitted as a first step and 3D classification with an initial Tel1 model ([Sawicka et al., 2016](#)), filtered to 60 Å, was performed instead for all datasets. Particle star files were sub-divided to speed up the processing pipeline, as the datasets still contained non-particles and 'junk' not removed by 2D classification. Initial 3D classification with 4 classes produced a single class (23% particles) that exhibited features expected for this protein. Similar 3D classes from each batch/dataset were selected, re-extracted twice binned, and joined before an initial consensus 3D refinement, which converged to 5.8 Å. After 3D refinement the particle stack was further cleaned using 3D classification in RELION-3.0 using local angular searches, higher T-factors (T=8) and sub-dividing into six classes. Of the 6 classes many displayed over-fitted and noisy features, however two classes (29%, and  $\sim 10\%$ ,  $\sim 160K$  and  $\sim 54K$  particles) showed clear secondary structure and internal features and were selected for further refinement. Particles corresponding to the best 3D classes were re-extracted (1.085 Å/pixel) in a slightly smaller box size (380 x 380 pixels) and were refined according to the gold-standard refinement procedure implemented in RELION-3.0 applying C2 symmetry and using a soft mask (C2 symmetric) corresponding to the protein. Beam-induced particle polishing ([Zivanov et al., 2019](#)) followed by CTF refinement ([Zivanov et al., 2018](#)) improved the map resolution producing a final map of the Tel1 dimer at 3.9 Å (class 01) and 6.0 Å (class03) according to the FSC = 0.143 criterion. Local resolution estimates calculated in RELION-3.0 showed that density regions corresponding to the N-terminal HEAT repeats were of lower resolution ( $\sim 5$  Å) as compared to the kinase-containing C-terminal half ( $\sim 3.6 - 4.4$  Å, [Figure S2A](#)). Using a soft mask (C2 symmetrized) encompassing some of the HEAT repeat regions, the FAT domain and the C-terminal kinase domain of the dimer, 3D refinement (gold-standard) improved the resolution yielding a 3.7 Å reconstruction after post-processing (according to FSC = 0.143 criterion) for Class01 and 4.7 Å after post-processing (according to FSC = 0.143 criterion) for Class03, corresponding to approximately two thirds of the protein. Angular accuracy and angular distribution plots suggest that rare views were captured by omitting initial 2D classification steps and that the early preferential orientation issues were circumvented as confirmed by directional FSC plots ([Tan et al., 2017](#)), demonstrating a reasonably isotropic reconstruction. An improved quality map corresponding to the kinase core was produced using signal subtraction in RELION-3.0, masking the HEAT repeat regions and refined (gold standard) masking the remaining kinase-M-FAT regions. This reconstruction was assessed to be 3.7 Å after post-processing (according to FSC = 0.143 criterion). Local resolution estimates show that the best resolution regions are better than 3.5 Å and the map shows defined secondary structure features and clearly resolved bulky side chains ([Figures S2 and S3](#)). A set of 167596 particles images ( $\sim 47\%$  from dataset 1,  $\sim 12\%$  from dataset 2,  $\sim 41\%$  from dataset 3) were used for the final reconstructions.

### Model Building and Refinement

The final 3.7 Å and 3.9 Å EM maps were sharpened with a negative B-factor of -200, as determined by RELION-3.0, or less to avoid high-resolution noise and therefore over fitting of a model. A structure of dimeric human ATM (pdb 5np0) was docked into the maps in the first instance. It was clear from this initial fitting that AMP-PNP was bound in the active site. The ATM model, which is restricted to C $\alpha$ -C $\beta$  only, was manually fitted as rigid body regions into our maps and residues that did not fit the density or that clearly differed between species were trimmed in Coot ([Emsley and Cowtan, 2004](#)). The high-resolution maps permitted accurate model building and therefore we built the structure manually starting with the kinase bound to AMP-PNP using the high-resolution nucleotide-bound X-ray structures of mTOR ([Yang et al., 2013](#)) and PKA ([Das et al., 2015](#)) as guides alongside side-chain density in our maps to model the correct location of the catalytic loop, activation loop and the glycine-rich loop. The kinase domain was subsequently built manually by using residues at the AMP-PNP bound active site as a start point and using bulky side chains as landmarks for correct

sequence assignment against UNIPROT accession code P38110. We also made use of a local agreement filtering program (Local Agreement Filtering Algorithm for Transmission EM Reconstructions [LAFTER]) (Ramlau et al., 2019) that produces a map filtered to maintain consistent features between the two independent half-maps from gold-standard refinement and recovers more signal. This allowed us to confidently place residues in loops and regions where sharpening did not aid model building. We were able to build co-ordinates with the majority of side chains corresponding to residues 1527-2787 and place residues with sequence assignment (but occasional side chains) to 967-1526. The N-HEATs were more challenging to build and so these were built as a poly-Alanine trace. The co-ordinates for the model corresponding to the FAT-Kinase regions of the dimer were first real space refined in PHENIX (Adams et al., 2010; Afonine et al., 2018) against the 3.7 Å map (sharpened with a B-factor of  $-165 \text{ \AA}^2$  for the FATKIN and  $-200 \text{ \AA}^2$  for the kinase core). The Tel1 Dimer co-ordinates (which include the previously refined FAT-Kinase region) were refined against the 3.9 Å map (sharpened with  $-75 \text{ B-factor}$ ). In both cases data used in refinement was limited to spatial frequencies estimated by RELION to prevent over-fitting. Ramachandran,  $C_\beta$ , non-crystallographic symmetry (NCS), and secondary structure restraints (generated in PHENIX using caBLAM) were used throughout the refinement to ensure good model geometry and the coordinates were validated using MOLPROBITY (Chen et al., 2015) in PHENIX. Typically 3-cycles of real space refinement were run (3 macro cycles of global and local optimization and B-factor refinement), with PHENIX automatically estimating relative weighting of the restraints and map to prevent over-fitting (Afonine et al., 2018). Refinement and model statistics are given in Table 1. Map vs model FSC curves were also generated in PHENIX as part of the refinement procedure and given in Figures S2 and S3.

### Model Interpretation and Analysis

Figures were created using PyMOL (Schrodinger, LLC) and UCSF Chimera (Pettersen et al., 2004). Structural superposition of structures was performed in PyMOL aligning kinases by their C-lobes. Dimer interface buried surface area estimates were calculated using PISA (Krissinel and Henrick, 2007). Multiple sequence alignments were performed using Clustal Omega (Sievers et al., 2011) and displayed in Jalview. Structure-based sequence alignments were performed in PROMALS3D (Pei and Grishin, 2007).

### QUANTIFICATION AND STATISTICAL ANALYSIS

CryoEM data were analysed and quantified using a Bayesian approach as described in RELION-3.0 (Zivanov et al., 2018). No statistical methods were used to predetermine sample size except sufficient images were collected to ensure adequate reconstructions could be obtained.

### DATA AND CODE AVAILABILITY

The cryoEM reconstructions and atomic co-ordinates generated in this study are available at the EMDDB under accession code EMD-10120 and the RCSB under the PDB code 6S8F.